PHYSICAL REVIEW B VOLUME 43, NUMBER 15 15 MAY 1991-II

# Electronic structure of $CrSi_2$ and related refractory disilicides

L. F. Mattheiss
*AT&T Bell Laboratories, Murray Hill, New Jersey 07974*
(Received 12 December 1990; revised manuscript received 19 February 1991)

The results of linear augmented-plane-wave band calculations for hexagonal $CrSi_2$, carried out in the local-density approximation, confirm that this compound is an indirect-gap semiconductor. The calculated indirect gap of 0.30 eV, which occurs within the Cr 3$d$ band manifold, is in excellent agreement with the measured optical value, 0.35 eV. However, the calculated onset energy for direct transitions (which are predicted to be polarization dependent) is about 0.2 eV below the observed ($\sim$0.67 eV) value. The corresponding calculated indirect gaps for the metastable hexagonal $MoSi_2$ (+0.02 eV) and $WSi_2$ (−0.03 eV) phases are diminished by chemically induced changes in the width and position of the $d$ bands relative to $E_F$. Similar effects produce a reduced ($\sim$0.22 eV) gap above $E_F$ for the isostructural group-V compound $VSi_2$. The transmission characteristics of a $CrSi_2$(0001)/Si(111) interface are analyzed in terms of the projected bulk $CrSi_2$ band-structure results.

Since most transition-metal silicides are metallic and form readily on silicon substrates, they have found important applications in silicon-based integrated-circuit technology as Schottky barriers and low-resistivity interconnects.[1] However, in early studies dating back to the 1960s, a few silicides have been identified as semiconductors, with typical band gaps in the 0.1–0.9-eV range.[2] These semiconducting silicides have attracted special attention in recent years because of their potential application as optoelectronic devices (such as light sources, infrared detectors, electro-optic interconnects, etc.) that can be fully integrated with current silicon microelectronic components.[3]

Among these semiconducting compounds, hexagonal $CrSi_2$ have been the most widely studied and best characterized material.[4] Nonetheless, there has not been universal agreement concerning its semiconducting nature.[5] In addition, it has been speculated[1] that "magnetic influences" may be responsible for its semiconducting properties. However, recent optical studies[6] on well-characterized thin-film $CrSi_2$ samples provide convincing evidence for both simple bandlike and semiconducting character. These measurements have shown that $CrSi_2$ exhibits an indirect band gap of about 0.35 eV. The data also indicate the onset of strong direct transitions near 0.67 eV.

Because of its potential importance in such novel device applications, there have been several efforts[7,8] to grow $CrSi_2$ epitaxially on the various faces of Si. Although the best quality interfaces have been achieved between (0001) $CrSi_2$ and (111) Si, the tendency to form $CrSi_2$ islands on Si has produced polycrystalline films with relatively small ($\sim$1–2-$\mu$m) grain sizes. A promising technique that may avoid these difficulties utilizes ion implantation to fabricate Si/$CrSi_2$/Si heterojunctions by inserting thin buried layers of $CrSi_2$ within Si(111) wafers.[9]

As a semiconductor, $CrSi_2$ is unique among the nine-member family of refractory disilicides $RSi_2$ (namely, those compounds containing $R$ =Ti, V, or Cr group elements). Unlike the well-studied group-VIII disilicides $CoSi_2$ and $NiSi_2$ that adopt the high-symmetry cubic fluorite structure, the refractory disilicides form with a variety of more complicated, low-symmetry orthorhombic ($C$54 structure, $R$=Ti; $C$49 structure, $R$=Zr, Hf), hexagonal ($C$40 structure, $R$=V, Nb, Ta, Cr), and tetragonal ($C11_b$ structure, $R$=Mo, W) structures. A unifying feature of these seemingly complicated phases is the fact that they each share a common structural element, namely, nearly hexagonal $RSi_2$ layers.[10] For example, the orthorhombic ($C$54), hexagonal ($C$40), and tetragonal ($C11_b$) phases can be generated simply by changing the stacking sequence (but not the registry) of neighboring $RSi_2$ layers. In particular, the orthorhombic $C$54, hexagonal $C$40, and tetragonal $C11_b$ structures contain four-layer ($ABCD$), three-layer ($ABC$), and two-layer ($AB$) stacking of nearly hexagonal $RSi_2$ planes. The orthorhombic $C$49 phase also involves a two-layer ($AB'$) sequence, though with different registry.

A second unique and unifying feature of the refractory disilicides is the fact that the transition-metal $d$ bands are situated near the Fermi level for this group of compounds.[11] The degeneracy of the $R$-atom $d$ states with the Si 3$p$ states optimizes the formation of strongly covalent $R$ $d$–Si 3$p$ bonds, which, according to the observed structural regularities, selectively enhance the stability of hexagonal $RSi_2$ layers. One expects that the overall progression from orthorhombic to hexagonal and finally to tetragonal structures is related to an increased filling of the $R$-atom $d$ manifold. The coexistence of both hexagonal $C$40 and tetragonal $C11_b$ phases among the group-VI compounds suggests a delicate balance between the structural energies for these phases. Indeed, metastable hexagonal $C$40 $MoSi_2$ and $WSi_2$ films have been formed using ion-implantation techniques and low annealing temperatures.[12] This suggests that the crucial stabilizing fac-

 ©1991 The American Physical Society

tor in hexagonal $CrSi_2$ may be related to the opening of a semiconductor gap at $E_F$ in this material.

In order to address these issues, the one-electron band structures for $CrSi_2$ and several related $RSi_2$ refractory compounds ($R$=V, W, and Mo) have been calculated in the local-density approximation (LDA) with the use of a scalar-relativistic version of the linear augmented-plane-wave (LAPW) method.[13] This implementation, which imposes no shape approximations on either the charge density or the potential, applies a rigid-core approximation to the tightly bound electrons while treating the Cr $3d^54s$ and Si $3s^23p^2$ states as valence electrons. Exchange and correlation effects are introduced with the use of the Wigner interpolation formula.[14] In the present study, the various LAPW computational parameters are identical to those utilized in a previous investigation[15] that focused on the sensitivity of the calculated $CrSi_2$ band gap to structural variations.

The primitive unit cell for the hexagonal $C40$ structure contains three $RSi_2$ formula units. The arrangement of the individual atoms in this primitive cell is shown in Fig. 1(a). The space group for this $C40$ structure is $P6_222$ ($D_6^4$), which is nonsymmorphic, containing nonprimitive translations ($\tau=c/3$ and $2c/3$) which interchange individual $CrSi_2$ layers in Fig. 1(a). The primitive vectors that generate the hexagonal Bravais lattice can be written

$$\mathbf{t}_1=(a/2)(\sqrt{3}\hat{\mathbf{i}}-\hat{\mathbf{j}}),\quad \mathbf{t}_2=a\hat{\mathbf{j}},\quad \mathbf{t}_3=c\hat{\mathbf{k}}\ . \tag{1}$$

The position coordinates of the Cr and Si atoms within the $C40$ primitive cell are listed in Table I. The reciprocal-lattice vectors that correspond to Eq. (1) are given by

$$\mathbf{b}_1=(4\pi/\sqrt{3}a)\hat{\mathbf{i}},\quad \mathbf{b}_2=(2\pi/\sqrt{3}a)(\hat{\mathbf{i}}+\sqrt{3}\hat{\mathbf{j}})\ ,$$
$$\mathbf{b}_3=(2\pi/c)\hat{\mathbf{k}}\ . \tag{2}$$

These generate the standard hexagonal Brillouin zone shown in Fig. 1(b). Athough the $D_6$ point group contains only half the full-hexagonal ($D_{6h}$) symmetry operations, $E_{n\mathbf{k}}$ exhibits full-hexagonal symmetry as a result of time-reversal invariance.[16]

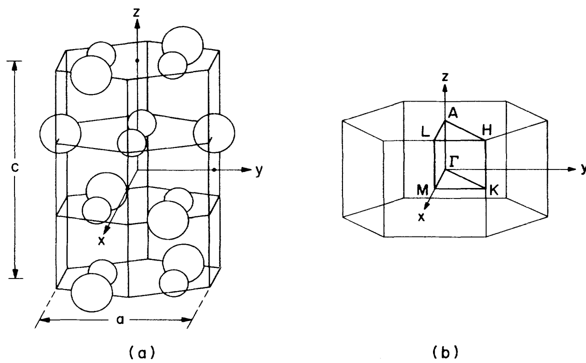


FIG. 1. (a) Primitive unit cell for hexagonal $C40$ $CrSi_2$, with large (small) spheres representing Cr (Si) atom positions. (b) Brillouin zone for hexagonal $CrSi_2$.

TABLE I. Internal atom-position coordinates $(\xi,\eta,\zeta)$ for hexagonal $C40$ $CrSi_2$ (space group $D_6^4$), in units of the primitive translation vectors $\mathbf{t}_1$, $\mathbf{t}_2$, and $\mathbf{t}_3$ of Eq. (1).

| Atom | Site | $\xi$ | $\eta$ | $\zeta$ |
|---|---|---|---|---|
| Cr | 3d | $\frac{1}{2}$ | 0 | $\frac{1}{2}$ |
| | | 0 | $\frac{1}{2}$ | $\frac{1}{6}$ |
| | | $\frac{1}{2}$ | $\frac{1}{2}$ | $-\frac{1}{6}$ |
| Si | 6j | $x$ | $2x$ | $\frac{1}{2}$ |
| | | $-x$ | $-2x$ | $\frac{1}{2}$ |
| | | $2x$ | $x$ | $\frac{1}{6}$ |
| | | $-2x$ | $-x$ | $\frac{1}{6}$ |
| | | $x$ | $-x$ | $-\frac{1}{6}$ |
| | | $-x$ | $x$ | $-\frac{1}{6}$ |

The near-neighbor bond distances at the Cr and Si sites in the $C40$ unit cell are listed in Table II, using the lattice-parameter values[17] ($a$=4.42 Å, $c$=6.349 Å) that have been applied in the present study. Apparently, there has not been a precise determination of the Si-atom position parameter $x$, since the quoted[17] $x=\frac{1}{6}$ value corresponds to the "ideal" geometry where each Cr and Si atom has six nearest neighbors ($d$=2.55 Å) within each hexagonal $CrSi_2$ layer. As discussed below, total-energy calculations show that the deviations from this ideal geometry are minimal, altering nearest-neighbor bond distances by less than 0.002 Å. In addition to their planar neighbors at $d$=2.55 Å, each Cr and Si is tetrahedrally coordinated with four interplanar neighbors ($d$=2.47 Å). The Cr sites have four Si interplanar neighbors while each Si site shares a pair of Cr and Si neighbors.

A novel characteristic of the orthorhombic ($C54$,$C49$), hexagonal ($C40$), and tetragonal ($C11_b$) phases of the refractory disilicides $RSi_2$ is the fact that each constituent is surrounded by a well-defined shell of ten nearest neighbors. Since these phases also exhibit comparable $R$—Si and Si—Si bond distances, they are especially suited for constituents with similar atomic sizes. The specific relationships between the lattice and atom-position parame-

TABLE II. Near-neighbor bond distances at the Cr and Si sites for hexagonal ($C40$) $CrSi_2$, with lattice parameters $a$=4.42 Å and $c$=6.349 Å and an "ideal" silicon position parameter, $x=\frac{1}{6}$.

| Atom | Neighbor | Number | $d$ (Å) |
|---|---|---|---|
| Cr | Si | 4 | 2.47 |
| | Si | 6 | 2.55 |
| | Cr | 4 | 3.06 |
| Si | Si | 2 | 2.47 |
| | Cr | 2 | 2.47 |
| | Si | 3 | 2.55 |
| | Cr | 3 | 2.55 |
| | Si | 4 | 3.06 |

ters that preserve these characteristics among the orthorhombic, hexagonal, and tetragonal phases are summarized in Table III.

With three formula units per primitive cell, one can anticipate a complicated valence-conduction energy-band structure that evolves from the 15 Cr 3*d* states and the 24 Si 3*s*,3*p* orbitals. This 39-band manifold spans an energy range of 20–25 eV, with the low-lying bands having predominant Si 3*s*,3*p* character (see Fig. 2 of Ref. 15). However, within the midst of this broad *d*-*p* complex, an energy gap of 0.30 eV is found to occur among the less dispersive Cr 3*d* states near $E_F$. This gap separates the highest filled valence-band states $E_{n\mathbf{k}}$ at $L$ ($n=21$) from the lowest unoccupied conduction band at $M$ ($n=22$). A detailed view of the $CrSi_2$ band structure near $E_F$ that emphasizes the Cr 3*d* orbital character in this energy range is shown in the upper portion of Fig. 2. Here, different symbols are used to distinguish the 3*d* orbitals with $d_{3z^2-r^2}$, $d_{xz,yz}$, and $d_{xy,x^2-y^2}$ symmetry. As indicated by the square symbols, the states near the valence-band maximum have predominant $d_{3z^2-r^2}$ symmetry while the conduction-band minima (triangles) at $L$ exhibit $d_{xz,yz}$ character. From the varied orbital character of the states near $E_F$, it is clear that the $CrSi_2$ band gap originates from a complicated combination of crystal-field splittings and hybridization effects within the Cr 3*d* manifold.

The present calculated value for the indirect $CrSi_2$ band gap, $E_{gap}=0.30$ eV, is in excellent agreement with the measured[6] optical gap of 0.35 eV. The analysis of transport data[18] yields a slightly smaller gap ($\sim$0.30 eV) that coincides with the present calculated value. This excellent agreement between the calculated LDA band gap and measured optical and transport values suggests that the well-known "band-gap" problem[19] is less severe in $CrSi_2$ than in typical tetrahedral *s*-*p* bonded semiconductors. As discussed previously,[15] the similar Cr 3*d* orbital characteristics of states on both sides of the $CrSi_2$ band gap may serve to minimize the nonlocal many-body corrections[20] to LDA in this system. The present LAPW results (particularly, the 0.30-eV band gap) are in contrast

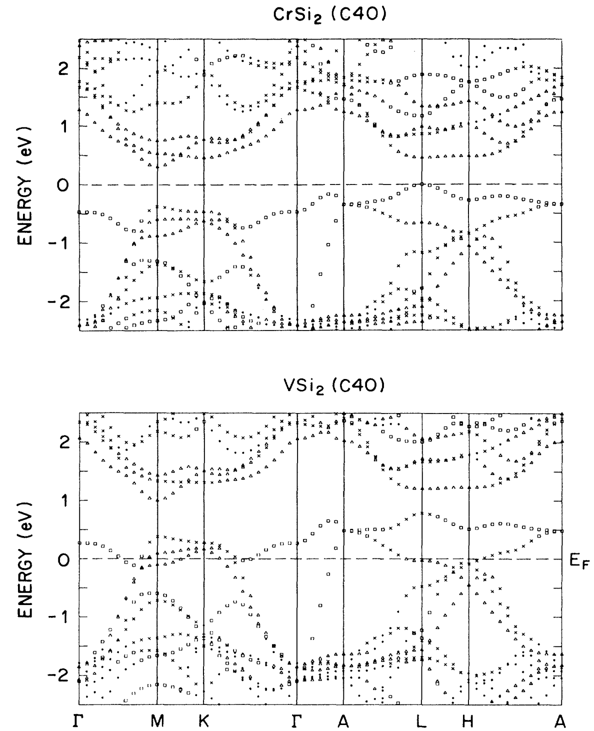


FIG. 2. LAPW energy-band results near $E_F$ for the hexagonal *C*40 phases of $CrSi_2$ and $VSi_2$. States with significant Cr 3*d* or V 3*d* orbital character are labeled with squares ($d_{3z^2-r^2}$ > 15%), triangles ($d_{xz,yz}$ > 30%), and *x*'s ($d_{xy,x^2-y^2}$ > 30%).

to those derived from previous extended-Hückel calculations,[5] where semimetallic properties have been predicted as a result of a slight band overlap ($\sim$0.1 eV) near the $M$ point in the Brillouin zone.

The $CrSi_2$ optical data[6] also suggest the onset of strong direct transitions near an energy of 0.67 eV. According to the present results, the lowest direct transitions (0.45 eV) occur at $L$ and involve states with $L_3$ (valence-band)

TABLE III. Comparison of model structural parameters for the various refractory-disilicide phases, with parameter values chosen to preserve the planar hexagonal $RSi_2$ geometry of the *C*40 structure. The lattice parameters for the model structures are denoted by primes, $d_i$ is the $RSi_2$ interlayer separation (with values appropriate for $CrSi_2$), and $u(R)$, $x$(Si), and $y$(Si) are "ideal" atom-position parameters.

| | *C*40 | $D^1_{6h}$ | $C11_b$ | *C*54 | *C*49 |
|---|---|---|---|---|---|
| $a'$ | $a$ | $a$ | $\sqrt{2}a/2$ | $\sqrt{3}a$ | $a$ |
| $b'$ | | | | $a$ | $\sqrt{3}a$ |
| $c'$ | $c$ | $c$ | $\sqrt{3}a$ | $4c/3$ | $2c/3$ |
| $d_i$ | $c/3$ | $c$ | $a/2$ | $c/3$ | $c/3$ |
| [Å] | [2.12] | [6.35] | [2.21] | [2.12] | [2.12] |
| $u(R)$ | | | | | $\frac{1}{12}$ |
| $x$(Si) | $\frac{1}{6}$ | $\frac{1}{6}$ | $\frac{1}{3}$ | $\frac{1}{3}$ | $\frac{9}{12}$ |
| $y$(Si) | | | | | $\frac{5}{12}$ |

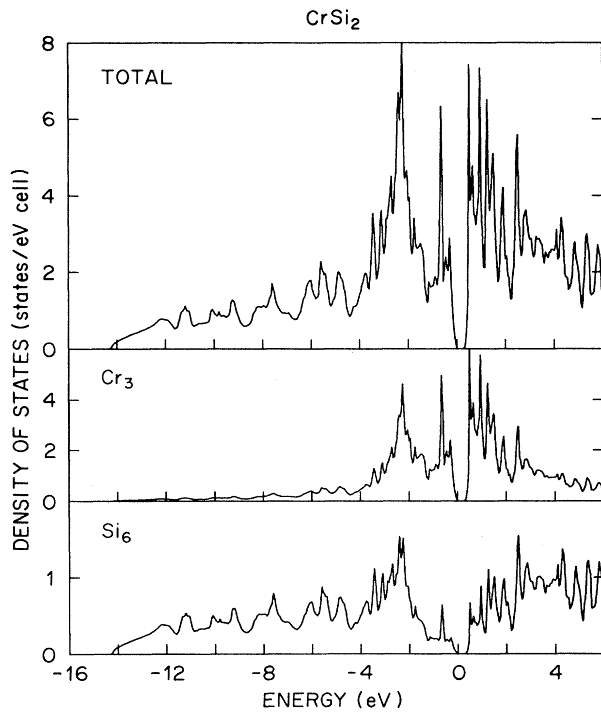


FIG. 3. Total and muffin-tin projected density-of-state results (per spin) for hexagonal $CrSi_2$.

and $L_1$ (conduction-band) symmetry.[21] Analysis of the selection rules[16] shows that this transition is allowed for electric polarization in the basal plane. The energy of these direct transitions increases monotonically along the $LM$ line from 0.45 to 0.68 eV; the latter energy corresponds to the $M_4 \rightarrow M_2$ transition, which is also dipole allowed for basal-plane polarization. These optical data suggest the possibility that matrix-element effects may enhance the direct transitions near $M$ relative to those at $L$. Clearly, future optical polarization studies are important since they would provide an additional test of the present calculated LAPW band results for $CrSi_2$.

Since the states at the valence-band maximum and conduction-band minimum are nondegenerate, it is straightforward to evaluate the effective masses for hole and electron carriers. It is found that the principal-axis components of the effective-mass tensor (i.e., those along the $LA$, $LH$, and $LM$ axes, etc.) are $(1.2,1.3,0.9)m_0$ and $(0.7,0.7,1.4)m_0$ for holes ($L$) and electrons ($M$), respectively. These values are substantially smaller than the corresponding empirical values [$\sim 3m_0$ (holes) and $\sim 20m_0$ (electrons)] that have been determined from the analysis of transport data.[18] In view of these large discrepancies, an independent determination of the $CrSi_2$ effective masses seems worthwhile.

A comprehensive overview of the $CrSi_2$ electronic structure is provided by the density-of-states results shown in Fig. 3. These density-of-states curves have been calculated with the use of tetrahedral interpolation, based on LAPW results at 76 uniformly distributed **k** points in the $\frac{1}{24}$ irreducible Brillouin-zone wedge shown in Fig. 1(b). The dominance of the Cr 3$d$ component near $E_F$ is reflected by the muffin-tin-projected results in the middle panel; here, the total density of states is weighted by the integrated LAPW charge within the Cr muffin-tin spheres. By comparison, the corresponding Si-projected results exhibit a roughly quadratic increase from the valence-band edge ($\sim -14$ eV), with a hybridization-

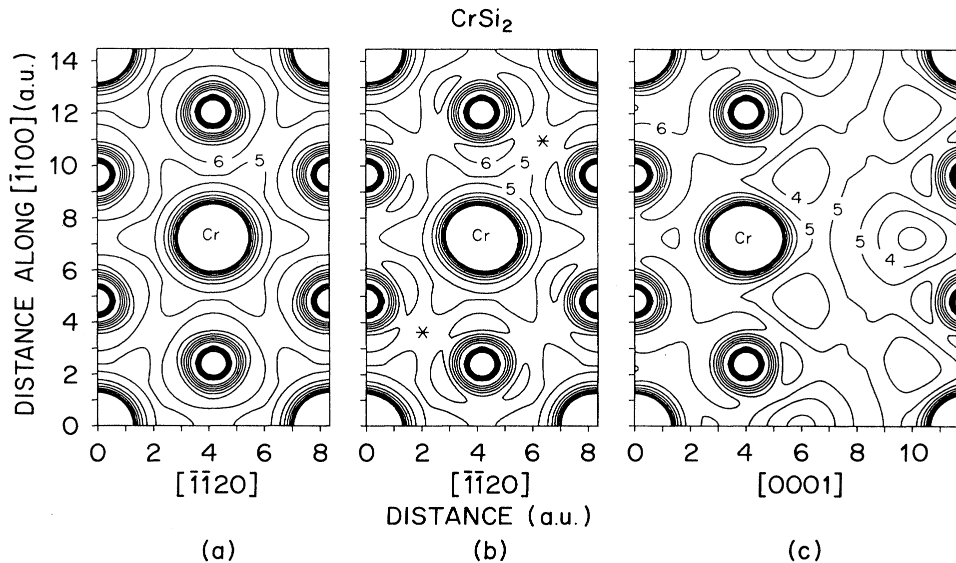


FIG. 4. LAPW valence-electron charge-density contours (in units $10^{-2}$ electrons/$a_B^3$) for hexagonal $CrSi_2$. The basal-plane results for a model single-layer phase ($D_{6h}^1$ symmetry) in (a) are compared with the corresponding $C40$ contours in (b); interlayer bonding for the $C40$ phase is illustrated in (c).

induced minimum near $E_F \approx 0$.

According to Fig. 3, the $CrSi_2$ valence-band density of states exhibits two main peaks at binding energies of 0.6 and 2.3 eV, respectively. These features are also seen in angle-integrated photoemission spectra for this compound.[5,11] The valence-band data at $h\nu = 50$ eV, which emphasize the Cr $3d$ component, exhibit two dominant valence-band features at binding energies of 0.6 and 1.7 eV, respectively. In agreement with the density-of-states curves of Fig. 3, the measured photoemission spectra contain little in the way of discernible structure at higher binding energies.

Some insight concerning the $CrSi_2$ bonding is provided by the contour plots of the LAPW valence charge density in Fig. 4. The results in Fig. 4(b) represent the charge density in a (0001) $CrSi_2$ layer of the $C40$ structure; the *'s label the primitive-cell origins. The charge density in a perpendicular $C40$ plane is illustrated in Fig. 4(c). For comparison, the somewhat simpler results in Fig. 4(a) have been determined from an analogous LAPW calculation for a model structure in which only one of the three $CrSi_2$ layers in the $C40$ primitive cell has been retained. The resulting simple-hexagonal structure with $D_{6h}^1$ symmetry (see Table III) contains well-separated ($\sim 6.3$-Å) $CrSi_2$ layers. In this case, the charge-density contours exhibit full-hexagonal symmetry.

Several noticeable changes are found in the corresponding $C40$-phase results in Fig. 4(b). The most obvious differences occur at the Si sites. Here, the nearly isotropic Si—Si and Si—Cr bonding in Fig. 4(a) is modified by the formation of strong interlayer Si—Si bonds, which have slightly shorter (2.47 versus 2.55 Å) bond lengths. The changes at the Cr sites are more subtle. In paricular, the innermost charge-density contours around the Cr exhibit slight nonspherical deviations that reflect changes in the Cr $3d$ band occupancy. In general, the $CrSi_2$ valence charge density in Fig. 4(b) is qualitatively similar to that exhibited by the pseudopotential results for tetragonal ($C11_b$) $MoSi_2$ and $WSi_2$ by Bhattacharyya *et al.*[22] In the body-centered-tetragonal $C11_b$ phase, the (110) plane corresponds to the (0001) plane of the hexagonal $C40$ structure.

The preceding results have been calculated assuming the "ideal" Si-atom position parameter $x = \frac{1}{6}$ (see Tables I–III). One can evaluate a theoretical value for this parameter by comparing the LAPW total energies as a function of $x$. The results of such calculations show that the deviation $\Delta x$ from the ideal $x = \frac{1}{6}$ value are minimal. In particular, a parabolic fit to the three calculated values of $E_{\text{val}}$ (relative to the minimum value $E_0$) for $\Delta x = -0.01$, 0.0, and $+0.01$ (0.107 917, 0.000 024, and 0.101 571 eV/formula unit, respectively) yields the small incremental shift $\Delta x = 1.5 \times 10^{-4}$. This correction to the ideal $x = \frac{1}{6}$ value changes the nearest-neighbor bond distances in Table II by less than 0.002 Å. Previous calculations[22] of the analogous Si-atom position parameter for the tetragonal $C11_b$ phase (see Table III) of the isoelectronic compounds $MoSi_2$ and $WSi_2$ have yielded similar results—namely, deviations from the ideal $x = \frac{1}{3}$ value which are small ($+0.0041$ and $+0.0033$, respectively) and positive. Although the calculated $CrSi_2$ band gap is extremely sensitive to the Si-atom position parameter,[15] the net correction to the calculated $CrSi_2$ gap shown in Fig. 2 is minimal ($\sim 1$ meV) because the calculated deviation $\Delta x$ is small.

As shown earlier,[15] the calculated $CrSi_2$ band gap is extremely sensitive to subtle structural variations that alter either the near-neighbor coordination geometry or the long-range (*ABC* versus *ABCD*) stacking sequence of $CrSi_2$ layers. One can expect a similar sensitivity to chemical effects which shift the position of the transition-metal $d$ bands relative to the Si $3s,3p$ bonding-antibonding complex and $E_F$. As shown in Fig. 5, the results of LAPW calculations for the metastable $C40$ phases of $MoSi_2$ and $WSi_2$ exhibit substantially reduced gaps of 0.02 and $-0.03$ eV, respectively. A comparison with the $CrSi_2$ results in Fig. 2 indicates an enhanced Si component among the valence- and conduction-band states near $E_F$.

Experimentally, the question as to whether the metastable hexagonal $C40$ forms of $MoSi_2$ and $WSi_2$ exhibit semiconducting or semimetallic behavior is presently unanswered. For example, the observation of a negative temperature coefficient of the resistivity in metastable thin-film samples of $MoSi_2$ (Ref. 23) and $WSi_2$ (Refs. 23 and 24) has received conflicting interpretations. On the

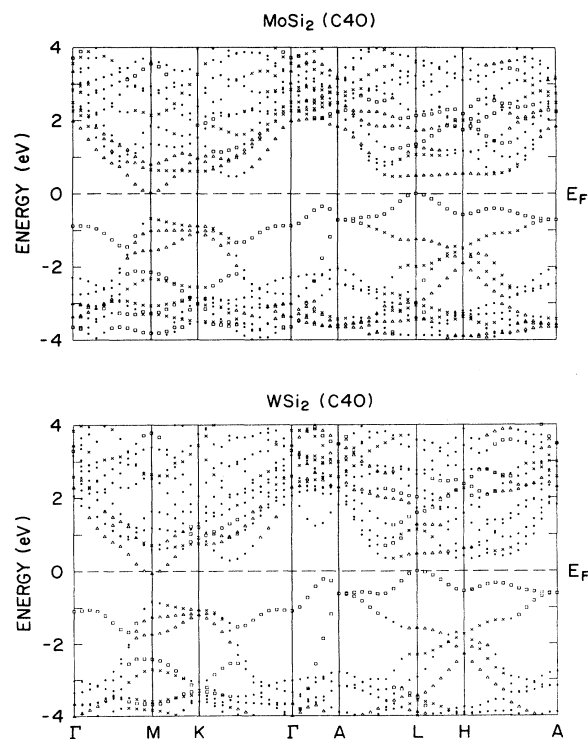


FIG. 5. LAPW results near $E_F$ for the metastable $C40$ phases of $MoSi_2$ and $WSi_2$. Bands with predominant Mo $4d$ and W $5d$ orbital character are labeled in accordance with Fig. 2.

one hand, this characteristic has been attributed[23] to the presence of a high density of stacking faults in these samples, which are typically annealed at relatively low ($\sim$550–600 °C) temperatures. However, an alternative interpretation[24] of similar $WSi_2$ data has led to the proposal that hexagonal $WSi_2$ is a semiconductor, with an estimated band gap of $\sim$0.4 eV. The results of the present calculations for $MoSi_2$ and $WSi_2$ support the former interpretation of these transport data, particularly in the case of $WSi_2$.

As shown in the lower position of Fig. 2, analogous calculations for the isostructural (*C*40) group-V refractory disilicide $VSi_2$ yield results near $E_F$ which are quite similar to those for $CrSi_2$. With three fewer valence electrons per primitive cell, the $VSi_2$ Fermi level is lowered below the $CrSi_2$ band gap, producing metallic behavior. A reduced gap of $\sim$0.22 eV remains in the energy range 0.8–1.0 eV above $E_F$. This gap, which is absent in earlier extended-Hückel results[25] for $VSi_2$, should be observable by means of inverse photoemission measurements.

Although potential device applications for $Si/CrSi_2/Si$ heterostructures are still in their early exploratory stages,[9] the present bulk $CrSi_2$ band-structure results can provide some theoretical insight concerning the expected transmission characteristics[26,27] of $CrSi_2/Si$ interfaces. The present analysis focuses on the most symmetrical interface involving the $CrSi_2$(0001) and Si(111) planes. The observed orientation[7,8] and likely registry of the uppermost hexagonal (0001) $CrSi_2$ layer with a (111) plane of Si atoms is shown in Fig. 6. The shaded Si-layer interface atoms occupy bridge sites between neighboring Si atoms in the $CrSi_2$ layer as well as an atop site above one-third of the interface Cr atoms. The net lattice mismatch is extremely small ($\sim$0.3%). As a result of this interface geometry, the primitive cell that preserves lateral translational symmetry at the interface is increased relative to the bulk for both constituents. A detailed analysis shows that the expanded Si cell contains four atoms per (111) layer while the corresponding $CrSi_2$ cell contains three formula units.

In order to achieve optimum transmission across a well-ordered epitaxial interface,[27] the incident and transmitted states on oppposite sides of the interface must share the same energy and parallel wave-vector component $\mathbf{k}_{\parallel}$. The introduction of superlattice effects at the interface complicates the identification of equivalent $\mathbf{k}_{\parallel}$ in the two bulk constituents. In the usual situation where Si is *n* type, $\mathbf{k}_{\parallel}$ is determined by the position of the conduction-band minimum along the $\Delta$ direction ($\sim 0.85\mathbf{k}_{\Gamma X}$) of the fcc Brillouin zone. (The corresponding results for *p*-type Si, where the valence-band maximum is at the zone center $\Gamma$, are readily obtained from this analysis.) For the hexagonal geometry that is appropriate for a (111) interface, the projected minima lie along the $\Gamma M$ directions of Fig. 1(b), near ($\sim 0.85\mathbf{k}_{\Gamma M}$) the zone boundary.

Because of the laterally increased Si and $CrSi_2$ primitive-cell dimensions at the interface, the identification of equivalent $\mathbf{k}_{\parallel}$ values for the two bulk phases involves successive folding and unfolding of their projected bulk Brillouin zones. The basic procedure is illustrated in Fig. 7. To the left, the open circles mark the location of the projected Si conduction-band minima ($\mathbf{k}_{\parallel} \approx \frac{5}{6}\mathbf{k}_{\Gamma M}$); the dashed lines define the surface of the (111)-projected bulk fcc zone. The solid lines identify the reduced (by a factor of $\frac{1}{4}$) Brillouin zone that is produced by the interface. As a consequence of superlattice effects, the folded minima (solid circles) have reduced wave vectors $\mathbf{k}_{\parallel} \approx \frac{1}{6}\mathbf{k}_{\Gamma M}$.

The analogous $CrSi_2$ results are shown to the right. Again, the solid lines outline the folded Brillouin zone of the interface while the dashed lines represent the boundary of the projected bulk Brillouin zone. After unfolding, it is found that the $\mathbf{k}_{\parallel}$ condition for *n*-type Si is satisfied for two wave vectors along the bulk $CrSi_2$ $\Gamma K$ direction, with magnitudes $\mathbf{k}_{\parallel} \approx \frac{1}{6}\mathbf{k}_{\Gamma K}$ and $\frac{5}{6}\mathbf{k}_{\Gamma K}$, respectively. For *p*-type Si, the corresponding $CrSi_2$ $\mathbf{k}_{\parallel}$ occur at $\Gamma$ and *K*.

In the case of a metal-semiconductor interface, the energy-matching condition can be estimated by using the observed Schottky-barrier height as a measure of band-bending effects near the interface.[26] The corresponding analysis for a semiconductor-semiconductor interface is more complicated since it depends on additional factors

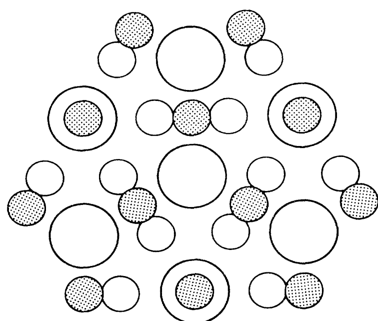

FIG. 6. The observed orientation and possible registry of $CrSi_2$(0001) and Si(111) atom planes (open and shaded circles, respectively) at a $CrSi_2$/Si interface.

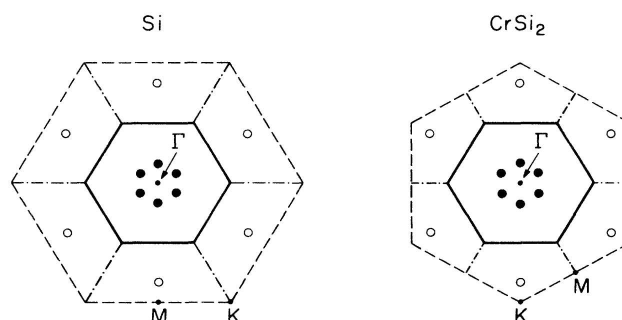


FIG. 7. Pictorial representation of the Brillouin-zone folding and unfolding that identifies equivalent $\mathbf{k}_{\parallel}$ in bulk Si and $CrSi_2$ for a $CrSi_2$(0001)/Si(111) interface (see text).

(such as the band lineup of the Si and $CrSi_2$ valence bands at the interface) which are presently unknown. However, the $CrSi_2$ band results of Fig. 2 show that possible energy-matching bulk states are generally available above the lowest conduction-band states ($\sim 0.5$ eV) near $K$. This low-energy cutoff is comparable to the observed[1] Schottky-barrier height ($\sim 0.6$ eV) for the ($n$-type) $Si/CrSi_2$ interface; this matching energy would be applicable in the limit $E_{gap} \to 0$.

For a $CrSi_2(0001)$ interface, the perpendicular wave vector $\mathbf{k}_\perp$ is along the $c$ axis. In Fig. 8, the bulk $CrSi_2$ band results near $E_F$ are plotted as a function of $\mathbf{k}_\perp$ for the pairs of $\mathbf{k}_\parallel$ values that are appropriate for $p$-type and $n$-type Si. As expected, energy-matching states are generally available above $\sim 0.5$ eV for both cases. Since the $\Gamma KHA$ plane does not possess reflection symmetry for the $C40$ structure, interface coupling is generally allowed for $n$-type Si. However, a quantitative understanding of the $Si/CrSi_2$ interface transmission characteristics will require a full dynamical calculation of the transmission and reflection coefficients.[27]

In summary, the results of LAPW band-structure calculations for hexagonal $CrSi_2$ confirm that this compound is an ordinary band-type semiconductor. The calculated band gap of 0.30 eV is in excellent agreement with the measured (0.35-eV) optical value. The predicted polarization dependence of the lowest-energy direct transitions should provide an important test of the calculated valence- and conduction-band states near $E_F$. Reduced gaps are predicted for the isostructural compounds $VSi_2$ ($\sim 0.22$ eV), $MoSi_2$ (0.02 eV), and $WSi_2$ ($-0.03$ eV).

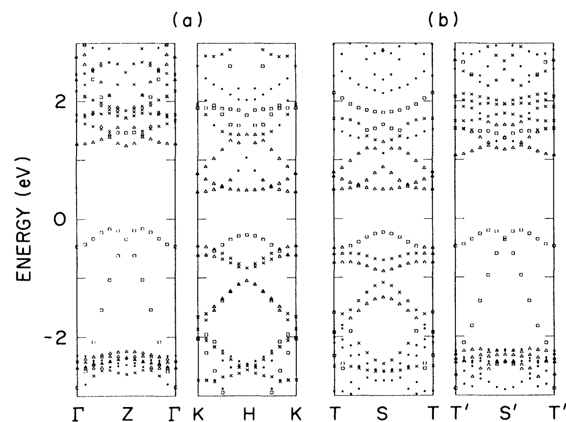


FIG. 8. Bulk $CrSi_2$ bands vs $\mathbf{k}_\perp$ for values of $\mathbf{k}_\parallel$ that are appropriate for (a) $p$-type and (b) $n$-type Si at a $CrSi_2(0001)/Si(111)$ interface. $T$ ($S$) designate points along the $\Gamma K$ ($AH$) lines ($T,S \Longrightarrow \frac{5}{6}$; $T',S' \Longrightarrow \frac{1}{6}$). Bands with predominant Cr $3d$ orbital character are labeled in accordance with Fig. 2.

I am pleased to acknowledge several valuable discussions with D. R. Hamann during the course of this investigation. I have also benefited from useful conversations with other colleagues, especially D. -J. Eaglesham, J. C. Hensel, T. Siegrist, R. T. Tung, and A. E. White. Finally, I am grateful to F. M. d'Heurle for bringing to my attention his work on the transport properties of metastable $C40$ $MoSi_2$ and $WSi_2$ thin films.

[1]S. P. Murarka, J. Vac. Sci. Technol. **17**, 775 (1980).
[2]G. V. Samsonov, *Handbook of High-Temperature Materials* (Plenum, New York, 1964), Vol. 2.
[3]M. C. Bost and J. E. Mahan, J. Vac. Sci. Technol. B **4**, 1336 (1986).
[4]M.-A. Nicolet and S. S. Lau, in *VLSI Electronics: Microstructure Science,* edited by N. G. Einspruch and G. B. Larrabee (Academic, New York, 1983), Vol. 6.
[5]A. Franciosi, J. H. Weaver, D. G. O'Neill, F. A. Schmidt, O. Bisi, and C. Calandra, Phys. Rev. B **28**, 7000 (1983).
[6]M. C. Bost and J. E. Mahan, J. Appl. Phys. **63**, 839 (1988).
[7]F. Y. Shiau, H. C. Cheng, and L. J. Chen, Appl. Phys. Lett. **45**, 524 (1984); J. Appl. Phys. **59**, 2784 (1986).
[8]R. W. Fathauer, P. J. Grunthaner, T. L. Lin, K. T. Chang, J. H. Mazur, and D. N. Jamieson, J. Vac. Sci. Technol. B **6**, 708 (1988).
[9]A. E. White, K. T. Short, and D. J. Eaglesham, Appl. Phys. Lett. **56**, 1260 (1990).
[10]F. Laves, in *Theory of Alloy Phases* (American Society for Metals, Cleveland, 1956), p. 181.
[11]J. H. Weaver, A. Franciosi, and V. L. Moruzzi, Phys. Rev. B **29**, 3293 (1984).
[12]F. M. d'Heurle, C. S. Petersson, and M. Y. Tsai, J. Appl. Phys. **51**, 5976 (1980).
[13]L. F. Mattheiss and D. R. Hamann, Phys. Rev. B **33**, 823 (1986).
[14]E. Wigner, Phys. Rev. **46**, 1002 (1934).
[15]L. F. Mattheiss, Phys. Rev. B **43**, 1863 (1991).
[16]M. Lax, *Symmetry Principles in Solid State and Molecular Physics* (Wiley, New York, 1974).
[17]W. B. Pearson, *A Handbook of Lattice Spacings and Structures of Metals and Alloys* (Pergamon, New York, 1958).
[18]I. Nishida and T. Sakata, J. Phys. Chem. Solids **39**, 499 (1978).
[19]L. J. Sham and M. Schlüter, Phys. Rev. Lett. **51**, 1888 (1983); Phys. Rev. B **32**, 3883 (1985).
[20]R. W. Godby, M. Schlüter, and L. J. Sham, Phys. Rev. Lett. **56**, 2415 (1986); Phys. Rev. B **36**, 6497 (1987).
[21]A. P. Cracknell, B. L. Davies, S. C. Miller, and W. F. Love, *Kronecker Product Tables* (Plenum, New York, 1979), Vol. I.
[22]B. K. Bhattacharyya, D. M. Bylander, and L. Kleinman, Phys. Rev. B **32**, 7973 (1985).
[23]C. Krontiras, I. Suni, F. M. d'Heurle, F. K. Le Goues, and R. Joshi, J. Phys. F **17**, 1953 (1987).
[24]F. Nava, B. Z. Weiss, K. Y. Ahn, D. A. Smith, and K. N. Tu, J. Appl. Phys. **64**, 354 (1988).
[25]O. Bisi and L. W. Chiao, Phys. Rev. B **25**, 4943 (1982).
[26]L. F. Mattheiss and D. R. Hamann, Phys. Rev. B **37**, 10 623 (1988).
[27]M. D. Stiles and D. R. Hamann, Phys. Rev. B **38**, 2021 (1988).